The importance of pre-existing fracture networks for fault reactivation during hydraulic fracturing

Nadine Igonin[1*], James P. Verdon[2], J-Michael Kendall[2], David W. Eaton[1]

1. Department of Geoscience, University of Calgary, Calgary, Alberta, Canada.

2. School of Earth Sciences, University of Bristol, Wills Memorial Building, Queen's Road, Bristol.

* Corresponding Author. Email: naigonin@ucalgary.ca, Tel: +1 403 542 7053.

ABSTRACT

Induced seismicity due to fluid injection, including hydraulic fracturing, is an increasingly common phenomenon worldwide. Yet, the mechanisms by which hydraulic fracturing causes fault activation remain unclear. Here we show that pre-existing fracture networks are instrumental in transferring fluid pressures to larger faults on which dynamic rupture occurs. To date, studies of hydraulic fracturing-induced seismicity have used observations from regional seismograph networks at distances of 10's km, and as such lack the resolution to answer some of the key questions currently in the field. A high-quality dataset acquired at a hydraulic fracturing site in Alberta, Canada that experienced several events over M_W 2.0 is presented for the purpose of analysing detailed mechanisms of fault activation. Both event hypocentres and measurements of seismic anisotropy reveal the presence of pre-existing fracture corridors that allowed communication of fluid-pressure perturbations to larger faults, over distances of up to a km or more. The presence of pre-existing permeable fracture networks can significantly increase the volume of rock affected by the pore pressure pulse, thereby increasing the probability of induced seismicity. This study demonstrates the importance of understanding the connectivity of pre-existing fracture networks as a tool for assessing potential seismic hazards associated with hydraulic fracturing of shale formations, and offers a conceptual understanding of induced seismicity due to hydraulic fracturing.

Plain language summary:

Felt earthquakes have been observed in North America, Asia and the U.K. during or shortly after hydraulic fracturing for shale gas development. An increase in fluid-pressure is widely accepted as the primary mechanism for fault activation, but current models cannot explain time delays (hours-to-days) and activation distance (up to a km) from the injection. Using high-resolution data acquired in close proximity to hydraulic-fracturing operations, we show that pre-existing fracture networks provide permeable conduits for diffusion of fluid pressure to a fault of sufficient size to host a felt earthquake. Our model explains both the observed time delay and activation distance and implies that mapping fracture networks may play a previously unrecognized important role in risk analysis for induced seismicity.

1. INTRODUCTION

The association of induced seismicity with hydraulic fracturing (HF) operations for shale gas extraction is now well-established (e.g., Atkinson et al., 2016; Bao and Eaton, 2016). For example, Kao et al. (2018) identified at least 5 instances in western Canada of M > 4.0 induced events, while notable cases of hydraulic fracturing-induced seismicity have been documented in Ohio (Friberg et al., 2014; Skoumal et al., 2015), Oklahoma (Holland, 2013) and the UK (Clarke et al., 2014). For most published case studies, seismicity is recorded using regional seismograph networks at distances of 10's km (or more), or local monitoring is installed after-the-fact once seismicity has started (e.g., Clarke et al., 2014; Darold et al., 2014; Friberg et al., 2014; Schultz et al., 2015a,b; Skoumal et al., 2015; Wang et al., 2016). With such limitations, further investigation into the causative mechanisms of induced seismicity is often not possible, meaning that different hypotheses cannot be conclusively tested (e.g., Deng et al., 2016; Schultz et al., 2017).

Debate persists about the relative contributions of pore-pressure increase or stress transfer in generating induced seismicity, as well as what trade-offs exist between these different mechanisms. Questions also continue about the distance from an injection site to which pore pressure or stress perturbations might be the dominant effect (Segall and Lu, 2015; Goebel et al., 2017), as well as the magnitude of perturbation necessary to trigger induced seismicity (e.g., Westwood et al., 2017; Wilson et al., 2018). Achieving a better understanding of the causative mechanisms will have significant implications for strategies used to mitigate induced seismicity. Where regulations pertaining to induced seismicity are applied, they are typically tailored toward reacting to cases of induced seismicity rather than prevention or mitigation (e.g., Green et al., 2012; Shipman et al., 2018). An improved understanding of the causes of induced seismicity may allow operators to characterise site-specific seismic hazards in advance during the site-selection phase and to have a better understanding of effective mitigation options at sites where induced seismicity does occur.

Here we use data from the Tony Creek dual Microseismic Experiment (ToC2ME) in the Duvernay shale, Alberta, an academic field experiment wherein hydraulic fracturing-induced seismicity was monitored using a purpose-built seismic network (Eaton et al., 2018). The largest events reached a magnitude of M_W = 3.2, and over 18,000 events were detected and located in the present study. Using this high-quality dataset we are able to investigate, in detail, the causative mechanisms for fault reactivation during hydraulic fracturing.

1.1. Potential Mechanisms for Fault Reactivation during Hydraulic Fracturing

Fault reactivation by subsurface human activities is usually characterised in terms of Mohr-Coulomb effects. The *in situ* stress field acting on a fault can be resolved into normal (σ_n) and shear (τ) stresses. If the effective shear stress exceeds the Mohr-Coulomb envelope given by:

$$\tau > \phi(\sigma_n - P) + C, \quad (1)$$

where P is the pore pressure, ϕ is the friction coefficient and C is the cohesion, then the fault will slip, causing seismicity. This equation is often re-formulated in terms of the Coulomb Failure Stress *CFS*:

$$CFS = \tau - \phi(\sigma_n - P), \quad (2)$$

where a positive change in *CFS* implies that the stress conditions are moving towards failure, and a negative change implies that the stress conditions are moving away from failure. The Mohr-Coulomb threshold may be reached in one of three ways (or a combination thereof): 1) an increase in the effective shear stress; 2) a decrease in the normal stress; 3) an increase in the pore pressure.

Figure 1 depicts some of the mechanisms by which fault reactivation may occur during hydraulic fracturing. An increase in pore pressure is a widely recognized causative mechanism for fault reactivation, since hydraulic fracturing, by definition, entails the injection of pressurised fluids into the subsurface. However, shale rocks have very low matrix permeability, meaning that elevated pressures will take a long time to propagate any distance away from the hydraulic fracture system that is in direct connection to the well (e.g., Atkinson et al., 2016). In most cases elevated pore pressures might not be expected to occur more than a few hundred meters from the injection point (e.g., Shapiro and Dinske, 2009).

Observations of fault reactivation occurring at larger distances has led some authors to suggest stress transfer as an alternative mechanism for fault reactivation (e.g., Westwood et al., 2017; Goebel et al., 2017). In this model, stresses transferred from pore-pressure into the solid matrix, or the deformation associated with tensile fracture opening and shear-slip on pre-existing fractures, will affect the stress field in the surrounding rocks and increase CFS. If the host medium has low permeability, then stress transfer through the rock frame might be expected to act over larger distances than the pressure pulse associated with injection (e.g., Deng et al., 2016). Alternatively, the presence of pre-existing fracture corridors within the shale may create local permeability enhancement, allowing elevated pore pressures to be transferred to greater distances. This mechanism has been proposed for several HF-induced case studies (e.g., Holland, 2013; Schultz et al., 2015a; Westaway, 2017).

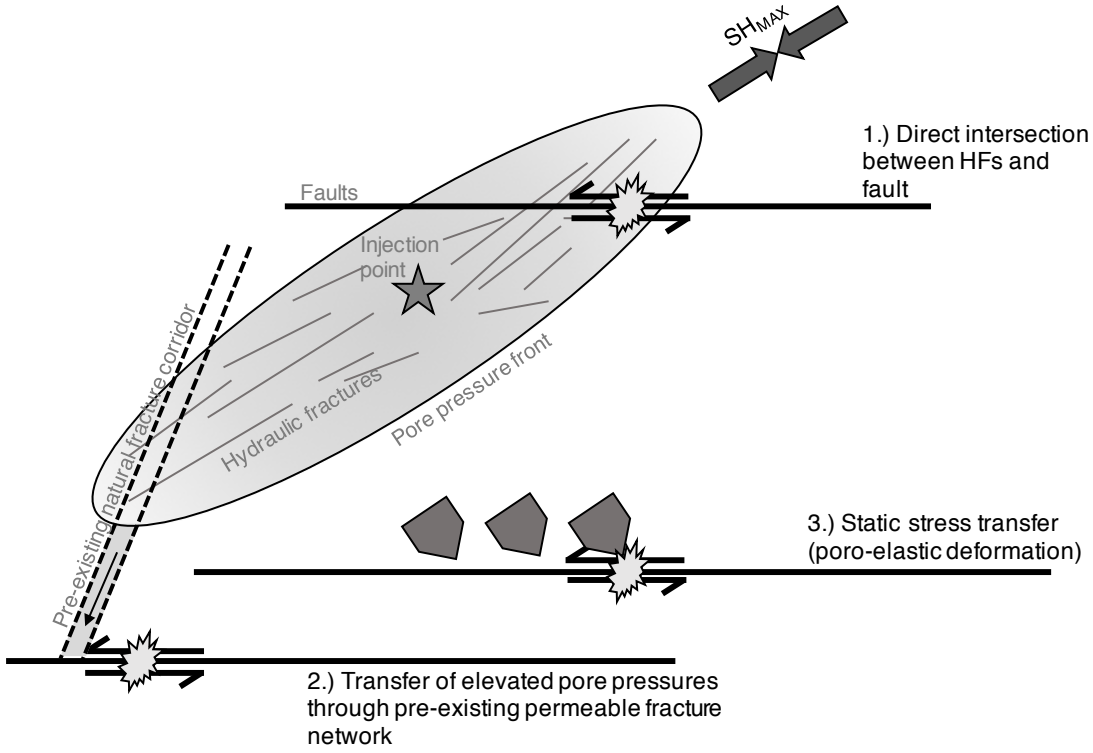

Figure 1: Schematic cartoon showing various mechanisms by which hydraulic fracturing may cause fault reactivation: 1) hydraulic fractures may directly intersect faults, 2) pre-existing permeable fracture corridors may transmit elevated pore pressures to a fault, and 3) stress transfer through the rock frame may increase the CFS acting on a fault.

In the following sections we introduce the ToC2ME dataset and examine in detail the processes that occurred as faults were activated, as illuminated by the hypocentres, timings and focal mechanisms of microseismic events. We combine these observations with both fluid flow and geomechanical modelling in order to understand which of the above mechanisms are causing fault reactivation.

2. DATA

The Tony Creek dual Microseismic Experiment was a research-focused field program acquired by the University of Calgary, using a suite of geophysical sensors to monitor hydraulic fracturing for shale gas. This dataset has already been the subject of several publications (Eaton et al., 2018; Igonin et al., 2018; Zhang et al., 2019). The site consisted of 4 horizontal wells drilled into the Duvernay Formation at approximately 3,400 m depth (Figure 2). The Duvernay Formation consists of a fine-grained organic-rich mudstone interfingered with carbonate. It is overlain by the Ireton Formation, which consists of 300 – 400 m of shales with organic content increasing with depth, and it is underlain by the Beaverhill Lake Group, which consists of

variability dolomitized carbonate platform and reef deposits. The crystalline Pre-Cambrian basement occurs at a depth of about 4000 m.

The wells were stimulated over a 4-week period in October – November 2016. Well C was stimulated first, from north to south along the well, after which the remaining wells were stimulated simultaneously in a "zipper-frac" process. In this study we focus on the events that occurred during stimulation of Well C. We do this because investigating and understanding the causes of fault reactivation is simpler early in the operation, during the initial stages of fault activation. Once faults have initially been reactivated, causative processes become more ambiguous, since it may not be possible to distinguish additional reactivation that is directly caused by later HF stages versus aftershock sequences that persist without any further anthropogenic contribution.

2.1. Event Detection and Location

The initial data acquisition and processing is described in detail by Eaton et al. (2018), and briefly reviewed here. The monitoring array consisted of 68 shallow borehole stations, with each station consisting of 3 vertical-component 10 Hz geophones placed at depths of 12, 17 and 22 m, and a 3-component 10 Hz geophone at 27 m. Additionally, 6 co-located broadband seismometers and 1 accelerometer were also installed at the surface.

Initial event detection was performed using an amplitude-based triggering algorithm to identify a set of template events. A matched-filter approach (e.g., Caffagni et al., 2016) was then used to detect smaller events. A relatively low detection threshold was used (Eaton et al., 2018), with the emphasis being on avoiding Type II errors (missed event detections). This produced a catalogue of over 25,000 putative event candidates. Eaton et al. (2018) used a relative location method to compute event hypocentres, but low signal-to-noise ratios meant that only 4,083 events could be robustly located. To improve the available catalogue, we therefore used the short-time/long-time averaging (STA/LTA)-based beamforming approach described by Verdon et al. (2017) to locate additional events. Applying quality-control criteria based on the observed stacking power, as described by Verdon et al. (2017), we successfully located 18,472 events. These events are mapped in Figure 2. The improvement in event detection produces a significant increase in the detail provided by the microseismic observations.

Many of the stages do not have any associated microseismicity. We infer from this that the microseismic events that are directly associated with hydraulic fracture growth (e.g., Eaton, 2018) are not visible given the estimated detection threshold of M_D = -0.2. This suggests that

159 the detected event clusters represent the activation of pre-existing features, such as fracture
160 corridors or faults, that can generate larger-magnitude events than the fracturing of intact rock.

161 In Figure 2 we categorise several event clusters that appeared during the stimulation of Well C.
162 Firstly, we consider a series of event clusters that intersect Well C with a trend of approximately
163 30^{o} – 210^{o}. We label these southwest-trending clusters SW1 – SW5, in sequence from north to
164 south along the well (in the order that they occurred during stimulation). Secondly, we see a
165 larger, linear cluster running north-south roughly 500 – 600 m to the west of Well C (labelled
166 NS1 in Figure 2), and a smaller N-S feature (NS2 in Figure 2) that is located between Wells C
167 and D.

168 The largest events (M_W = 3.2) all occurred within the large, N-S trending NS1 feature. The
169 Gutenberg and Richter (1944) *b*-values are b = 1.12 for NS1 and b = 1.10 for NS2 (Igonin et
170 al., 2018). In contrast, the *b*-values for the SW-trending clusters are higher: b = 2.54 for the NE
171 portion of SW1 and b = 2.18 for the SW portion of SW1, and b = 1.82 for SW2, SW3 and SW4
172 combined (Igonin et al., 2018). Our inference is that the NS1 and NS2 features represent larger
173 rupture planes, i.e. faults, whereas the SW1 – SW5 features represent corridors with a more
174 distributed array of interconnected fractures in which events are smaller, with a higher *b*-value
175 (e.g., Verdon et al., 2013).

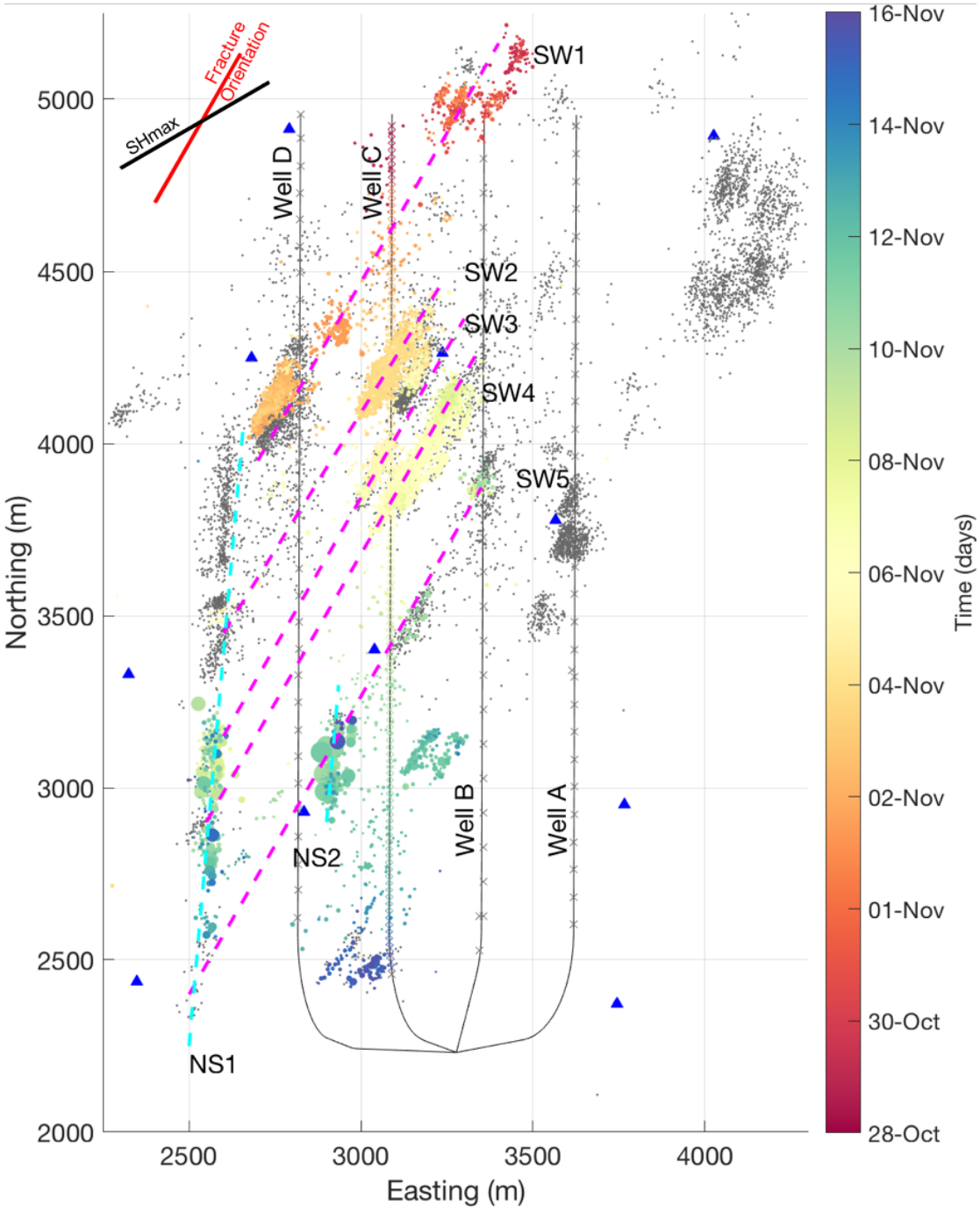

176

177 *Figure 2: Map of events recorded during hydraulic stimulation of Well C (dots coloured by occurrence*
178 *time) and during stimulation of Wells A, B and D (black dots) recorded during stimulation of Well C at*
179 *the ToC2ME site. Well C is the first to be stimulated, with hydraulic fracturing treatments taking place*
180 *along its full length. Features delineated by the microseismic activity are annotated: the large, N-S*
181 *trending fault NS1 runs roughly 500 m to the east of Well C, while a smaller N-S fault NS2 is closer to*
182 *Well C towards its heel. Five discrete clusters trending at 30° (SW1 – SW5) are identified, which extend*
183 *to both the east and west of Well C.*

184 **2.2. Determination of principal stress direction**

We begin our assessment of *in situ* stress conditions using World Stress Map (WSM) data (Heidback et al., 2016). On a regional scale in Alberta, there is a generally uniform maximum horizontal stress direction of 45° < $\theta_{S_{Hmax}}$ < 47°. However, in the Fox Creek area specifically, the $\theta_{S_{Hmax}}$ orientation varies from 44°-64°. One of the likely reasons for this variability is the proximity to reef edges, which have been shown in previous studies to have a significant control on the stress field orientation (e.g. Viegas et al., 2018). Since our dataset was acquired within a few kilometres of known reef edges, additional data was used to determine the local stress conditions.

Zhang et al. (2019) computed focal mechanisms for a subset (530 events) of the ToC2ME dataset (Figure 4). For the events in clusters NS1 and NS2 they found right-lateral strike-slip mechanisms, with one of the nodal planes oriented N-S, while for the events in the SW1 – SW5 clusters they found right-lateral strike slip mechanisms with one of the nodal planes oriented at 30°. The nodal plane strikes are consistent with the orientations of the event clusters. Zhang et al. (2019) used these focal mechanisms to estimate the *in situ* stress field using a linear stress inversion method (Michael, 1984), finding $\theta_{S_{Hmax}} \approx 60°$. This value is 15° from the regional stress direction, but lies within the range of WSM stress orientations observed in the local area.

We do not observe clusters of microseismicity that are aligned close to the SHmax direction, which is the expected orientation for operationally induced microseismicity during hydraulic fracturing (e.g., Eaton, 2018). Thus, as outlined above we infer that the microseismicity that is directly associated with hydraulic fracturing falls below the detection limits of the methods used here. In contrast, when hydraulic fractures intersect faults or fracture corridors this gives rise to larger, detectable events, with both the cluster orientation and the focal mechanisms aligned along the orientation of the activated feature.

2.3. Imaging fracture networks using seismic anisotropy

To image the seismic anisotropy at the site we used the method of Teanby et al. (2004) to measure S-wave splitting on the 300 largest-magnitude events, since these had the best signal to noise ratios, and clear P- and S-wave picks on all or most stations. We made a total of over 20,000 individual S-wave splitting measurements (300 events recorded at 69 stations), but quality-control criteria (Teanby et al., 2004) reduces this to a population of 7,818 good quality measurements.

The fast S-wave orientations, ψ, are plotted at each receiver (although they actually represent the path-averaged anisotropy between their respective sources and receivers) in Figure 3. There

is variation in ψ over the array footprint, with ψ oriented N-S to the south east of the array, but becoming more E-W to the NE of the array. However, around the wells themselves, ψ is relatively consistent at approximately 30°. This is a close match to the orientations of the SW1 – SW5 clusters, inferred earlier to be fracture corridors. It is roughly 30° from the estimated $\theta_{S_{Hmax}}$ orientation of 60°. We interpret the fast S-wave ψ = 30° as being caused by pre-existing fracture networks within the Ireton formation oriented in this direction. At 30 degrees from $\theta_{S_{Hmax}}$, these parallel fracture sets are optimally oriented for failure.

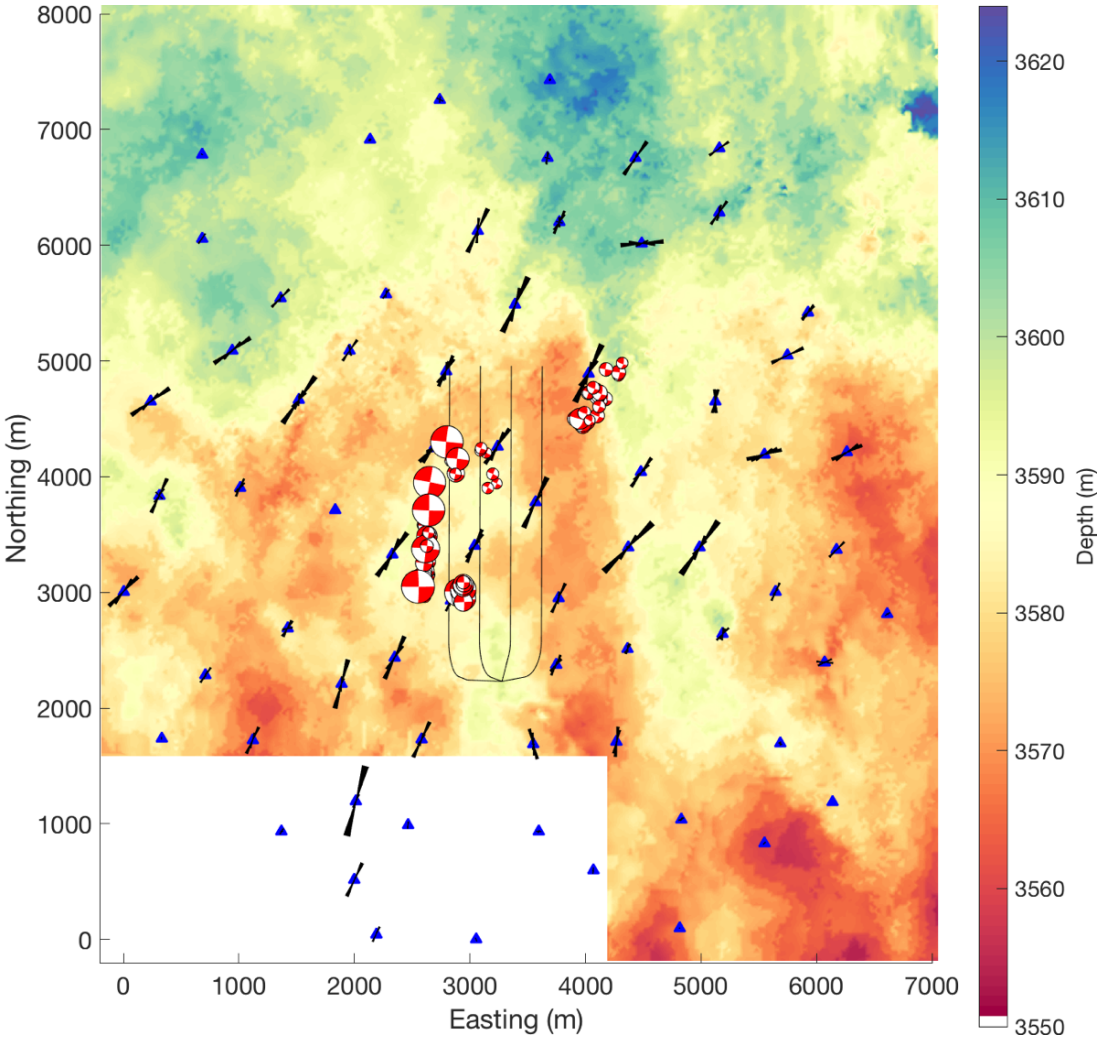

Figure 3: Map view of anisotropy observed using S-wave splitting analysis. Fast S-wave directions are plotted as rose diagrams at each station and focal mechanisms for the 100 largest events are shown at their respective event locations. Background contours show the depth structure of the Beaverhill Lake Group formation. Focal mechanisms for a subset of events computed by Zhang et al. (2019) are also shown.

A 3D/3C reflection seismic survey acquired at the site provides further information about faults at the site. Figure 3 shows the depth to the top of the Beaverhill Lake Group formation, which underlies the Duvernay. Significant depth discontinuities mark the positions of dip-slip faults that extend from the Pre-Cambrian basement through to the Duvernay (Eaton et al., 2018). In particular, a large fault trending roughly N-S can be seen just to the east of Well A. It is rooted in the basement, and is thought to be formed during extensional rifting in the Precambrian age (Ekpo et al., 2017). However, this feature does not appear to re-activate during injection. Based on the depths obtained for the 18,000 events, there appears to be no indication of rupture extending into the basement (see Supplementary Material). In fact, all of the large events are concentrated in the Ireton formation. This behaviour contrasts with induced earthquakes in Oklahoma and Ohio, where the largest earthquakes have been shown to occur in the basement, both due to wastewater injection (Ellsworth, 2013), and hydraulic fracturing (Kozłowska et al., 2018).

3. Interpretation: Position and Timing of Fault Reactivation

We evaluate fault activation by examining the timing and position of reactivation within the various clusters relative to positions of HF stages (Figure 4). An animation of the whole sequence is provided in the Supplementary Materials. In addition to the observed microseismic events, we plot ellipses with a long axes oriented at 60^{o}, centred on each perforation interval. These are included to delineate the assumed positions of the hydraulic fractures themselves, which are not directly imaged by the microseismic events. The key events within the sequences of microseismicity are also listed in Table 1.

Time	*Stage No.*	*Processes*
Oct 31st, 23:00	7	Activity begins in SW1 cluster
Nov 2nd, 23:00	29	Activity begins in SW2 cluster
Nov 4th, 18:00	47	Activity begins in SW3 cluster
Nov 4th, 20:00	48	Activity begins on the NS1 fault, at a position in line with the SW2 cluster
Nov 5th, 07:00	53	Activity begins in the SW4 cluster
Nov 7th, 10:00	64	Activity on the NS1 fault shifts southward to a position in line with the SW3 cluster
Nov 8th, 18:00	73	Activity begins in the SW5 cluster
Nov 9th, 03:00	77	Activity on the NS1 fault shifts southward to a position in line with the SW4 cluster
Nov 9th, 23:00	87	Activity begins on the NS2 fault where it is intersected by the SW5 cluster

Nov 12th, 20:00	115	Activity on the NS1 fault shifts southward to a position in line with the SW5 cluster.

Table 1: Sequence of processes that occur during the stimulation, as illuminated by the microseismicity.

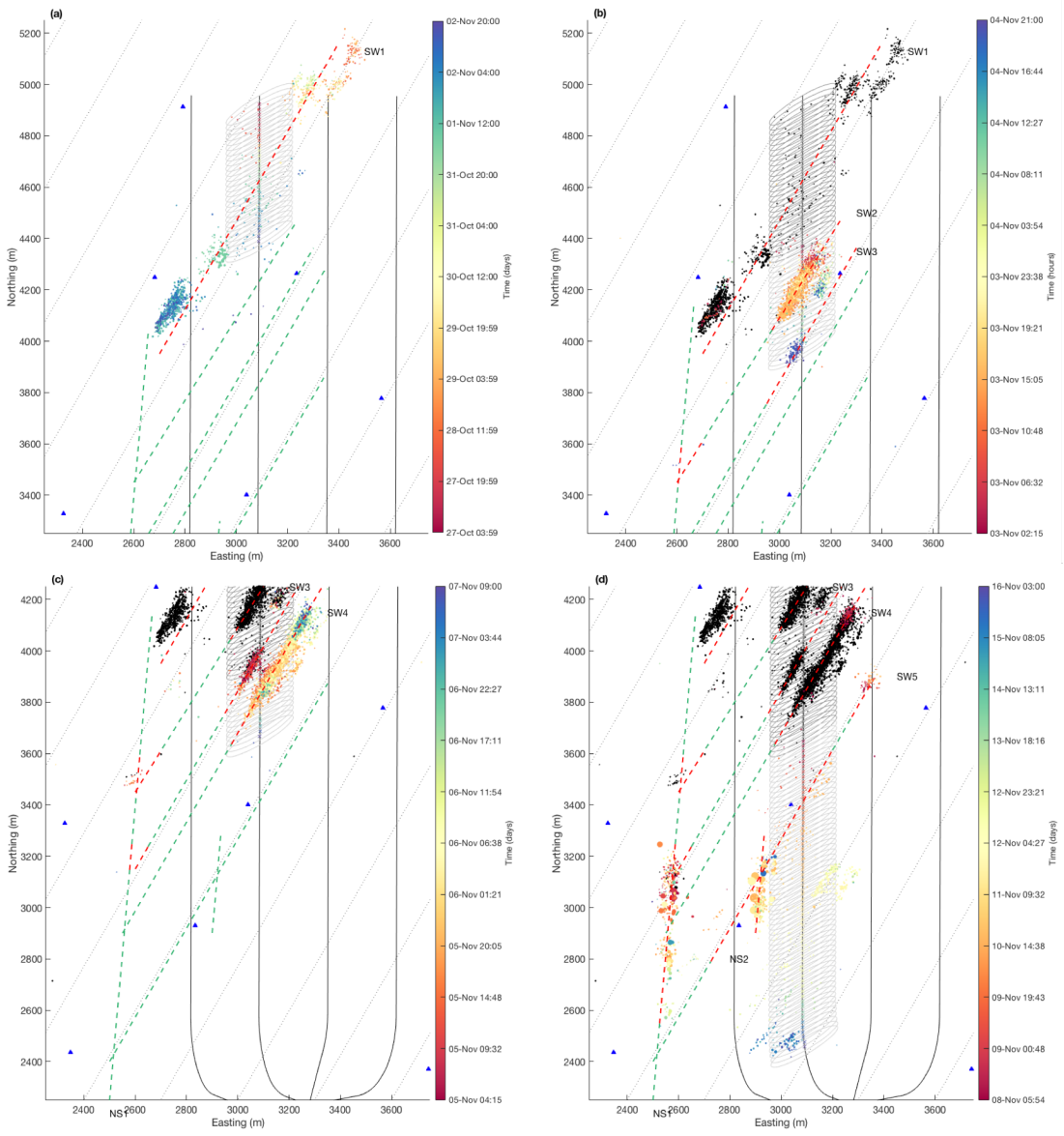

Figure 4: Snapshots of activity along well C. (a) Stages 1-28, (b) stages 29-49, (c) stages 50-64, and (d) stages 65-125. Black dots show the events that had occurred before this time, coloured dots show events that occurred during the specified time period. The SW and NS clusters are highlighted by dashed line, which are coloured red when events are observed on them (and green before this). The grey ellipses show the assumed positions of the hydraulic fractures (trending parallel to $\theta_{S_{Hmax}}$, with a length of 150 m) from each stage.

Figure 4a shows events that occurred during Stages 1-28. During this time, events occur in the SW1 cluster. The southernmost tip of SW1 does not quite reach NS1, and no events are observed along NS1 at this time.

Figure 4b shows Stages 29 to 48. At this time, the SW2 cluster is activated, and activity has also initiated in SW3. The first events on the NS1 fault are also seen at this time. The positions of these first events on the NS1 fault are aligned with the SW2 cluster, i.e. they occur at the point at which a continuation of the SW2 cluster would intersect the NS1 fault. The lateral distance from the active stage at this time, Stage 48, to the first NS1 events is approximately 800 m, and these NS1 events do not align with a continuation of the Stage 48 position along the $\theta_{S_{Hmax}}$ direction.

Figure 4c (Stages 49 to 64) shows similar behaviour. Activity continues in the SW3 cluster, and begins in the SW4 cluster as it is intersected by the stimulation zones. From Stage 64 onwards the NS1 fault is activated again, with events now occurring several hundred meters south of where the original activation began. The new locus of reactivation on NS1 is aligned with the SW3 feature, and is approximately 900 m from the position of the active stage. Again, the events do not align with a continuation of the active stage position along the $\theta_{S_{Hmax}}$direction.

Figure 4d shows the remaining the activity from Stages 65 to 125. Activity in the SW5 cluster begins during Stage 73 as it is intersected by the stimulation. The NS2 fault begins to reactivate during Stage 87, and the loci of the initial events on NS2 is aligned with the SW5 cluster. The locus of activity on NS1 continues to shift southward, and from Stage 115 onwards another burst of events occurs on the NS1 fault in a position that is aligned with the SW5 cluster.

In summary, the timing and position of the seismicity on the NS1 fault appears to be controlled by the positions of the SW-trending fracture corridors. The SW1 cluster does not appear to reach the NS1 fault, and no activity associated with this feature is observed on NS1. When the NS1 fault does begin to activate, it does so in a position that is directly aligned with the SW2 cluster. Subsequently, the loci of activity shifts southwards along NS1, and each shift in position is to a new locus that is aligned with each of the SW clusters.

We infer that the SW2 – SW5 fracture corridors represent permeable pathways, transmitting elevated pore pressures from the well to the NS1 and NS2 faults. There is a time delay between the activation of each SW cluster at the well, and the occurrence of seismicity at the corresponding position on NS1 (see Table 2). This time delay may correspond to the time

elapsed as elevated pressures propagated along the SW-trending fracture corridors, reaching and reactivating the NS1 fault.

	Time activation begins at well	Time activation on corresponding part of NS1 begins	Time delay (hours)
SW1	Oct 31st, 23:00	NA	NA
SW2	Nov 2nd, 23:00	Nov 4th, 20:00	44
SW3	Nov 4th, 18:00	Nov 7th, 10:00	64
SW4	Nov 5th, 07:00	Nov 9th, 03:00	92
SW5	Nov 8th, 18:00	Nov 12th, 20:00	98

Table 2: Delay times between the onset of activity in each of the SW clusters, and the onset of activity on the corresponding segments of the NS1 fault.

4. Investigating Possible Mechanisms for Fault Reactivation

4.1. Fluid-flow modelling

To investigate whether fluid flow along pre-existing fracture corridors is a plausible mechanism for fault reactivation, we model the expected diffusion of pressure along a fracture corridor. Initially we approach the problem analytically, using the concept of seismic diffusivity. Talwani and Acree (1985) studied a series of reservoir-impoundment induced earthquakes. Their observations of delay times between reservoir lake levels and seismicity, and of increasing epicentral areas with time, led them to conclude that pore pressure diffusion was the causative mechanism. They applied the concept of seismic hydraulic diffusivity, α_s, which describes the relationship between the event occurrence time t, and the distance between the event and the pore pressure source L:

$$\alpha_s = \frac{L^2}{t}. \quad (3)$$

Along the 30° orientation mapped by the SW clusters, the NS1 fault is located roughly 800 – 1,000 m from Well C. The events on the NS1 feature commence from between 44 to 98 hours after activation of each of the respective SW clusters (Table 2). Using these parameters in Equation 2, we arrive at values of $2.8 < \alpha_s < 7$ m^2/s, well within the range of values described by Talwani and Acree (1985), who found values of $0.5 < \alpha_s < 60$ m^2/s for a variety of geological settings, with most values clustering around 5 m^2/s.

The permeability of a fracture corridor, κ_{FC}, can be computed from the diffusivity using (Brace, 1980):

$$\kappa_{FC} = \frac{\alpha_s \eta \phi}{K}, \quad (4)$$

where η is the fluid viscosity, ϕ is the porosity, and K is the fluid bulk modulus. Because we do not know whether the fracture corridors are saturated with gas or water, we consider both cases, using the Batzle and Wang (1992) equations to compute the properties of gas with a specific gravity of 1, and brine with a salinity of 100,000 ppm, at a temperature of 100ºC and a pressure of 38 MPa, and use a value for porosity of $\phi = 6.5\%$. These values are a very generic representation of conditions in the Ireton (e.g., Dunn et al., 2012; Lyster et al., 2017). Use of these values in Equation 4 yields an analytic solution with values of κ_{FC} varying from 25 – 100 mD.

To incorporate greater complexity including multiple phases of injection at different times and locations we address the problem numerically using a commercial reservoir simulation code Tempest (Emerson, 2014). We create a model that represents our inferred system – hydraulic fractures intersecting a fracture corridor that transfers pressure increases – in a simplified form. Tempest simulates fluid flow through porous systems but does not simulate the coupled hydro-geomechanical behaviour of HF propagation. Instead, we pre-insert the hydraulic fractures and a fracture corridor into the model. This simplification is reasonable because our primary aim is to model fluid and pressure propagation along a pre-existing fracture corridor, rather than to simulate the HF propagation itself. Whereas developing a hydro-geomechanical simulation is complex from a modelling perspective, reservoir fluid flow models are relatively simpler to populate and utilise. Similarly, while in reality the permeability of a fracture corridor will be pressure-dependent, we do not simulate this effect in our model.

The model setup is shown in Figure 5. The background shale rock has a permeability of κ_S = 0.005 mD (Ghanizadeh et al., 2015a). We simulate 11 individual HF stages with a horizontal spacing of 20 m, representing roughly the number of stages that appear to be associated with reactivation of each SW-trending fracture corridor based on the observed microseismicity. Based on the operational records (Eaton et al., 2018), we model 400 m^3 of water injected over a 3-hour period for each stage, with a 1 hour gap between each stage. Each stage connects to a HF with a permeability of 1,000 mD, a half-length of 150 m and a height of 120 m, running at 60º to the well trajectory. The fracture corridor has a length of 1,200 m, width of 5 m, and a height of 300 m, running at 30º to the well trajectory. The fracture corridor is intersected by each of the hydraulic fractures that extend from the well. Using our analytical results as a

starting point, we vary κ_{FC} from 50 – 1,000 mD. Full model details are provided in the Supplementary Materials.

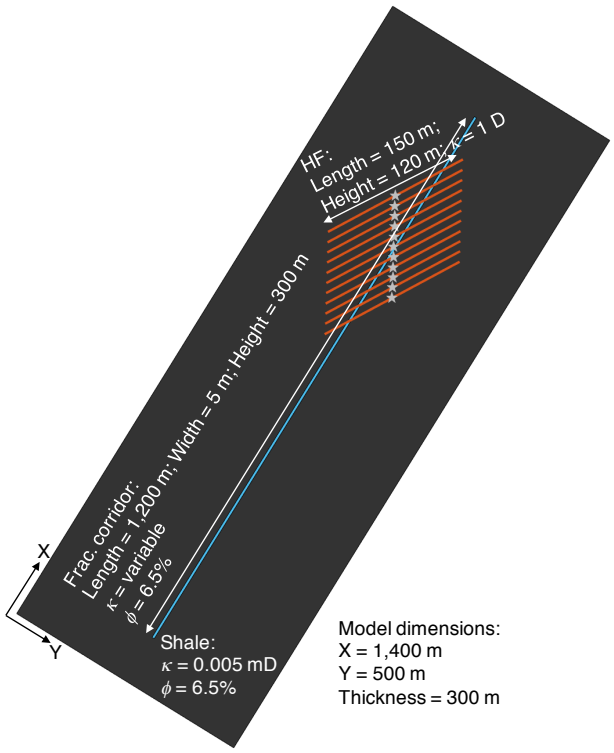

Figure 5: Schematic representation of our fluid flow model: 11 HF stages (red lines) are simulated, which connect into a fracture corridor (blue line) with a length of 1,200 m and a width of 5 m.

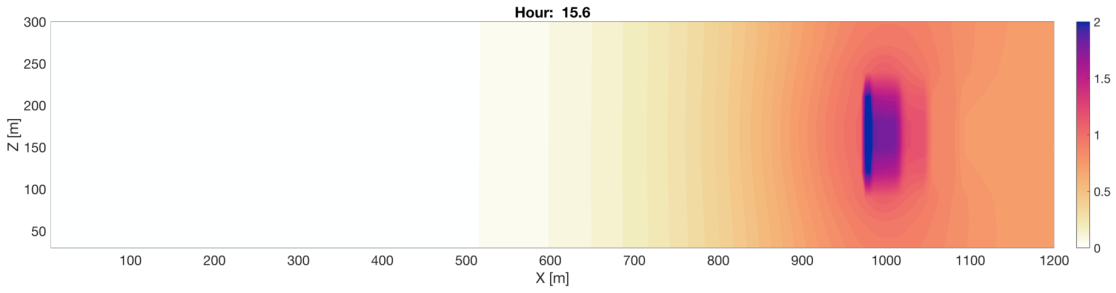

Figure 6: Modelled change in pore pressure (in MPa) at a single time-step (T = 15.6 hours) along the fracture corridor: pressures are elevated where the HF intersects the fracture corridor (at X = 980 m), and propagates along the feature.

Figure 6 demonstrates an example model instantiation (κ_{FC} = 100 mD), showing the distribution of pore-pressure changes along the fracture corridor at a single model time-step (an animation showing the pressure evolution along the fracture corridor as a function of time is provided in the Supplementary Materials). Pressures become elevated where the active HF intersects the fracture corridor – this pressure pulse then propagates along the length of the fracture corridor.

Our primary interest is the pressure change at the distal end of the fracture corridor, where it would intersect the NS1 fault. In particular, we are interested in the magnitude of any pressure increase, and its timing relative to the injection stages, as this will indicate whether (i) the modelled pressure changes are sufficient to cause fault reactivation, and (ii) whether the timing of pressure increase is commensurate with the observed time delays between initial reactivation of the SW clusters near to the well and the onset of activity on the NS1 fault.

Figure 7 shows our results, with the curves representing models with varying values of κ_{FC}. In each case we observe an increase in pressure, the magnitude and timing of which is strongly dependent on the fracture corridor permeability. The magnitude of the pressure increase, ΔP_{MAX}, is larger for higher permeabilities, with the largest increase of $\Delta P_{MAX} = 0.85$ MPa occurring for $\kappa_{FC} = 1{,}000$ mD, and the smallest increase of $\Delta P_{MAX} = 0.45$ MPa occurring for $\kappa_{FC} = 50$ mD.

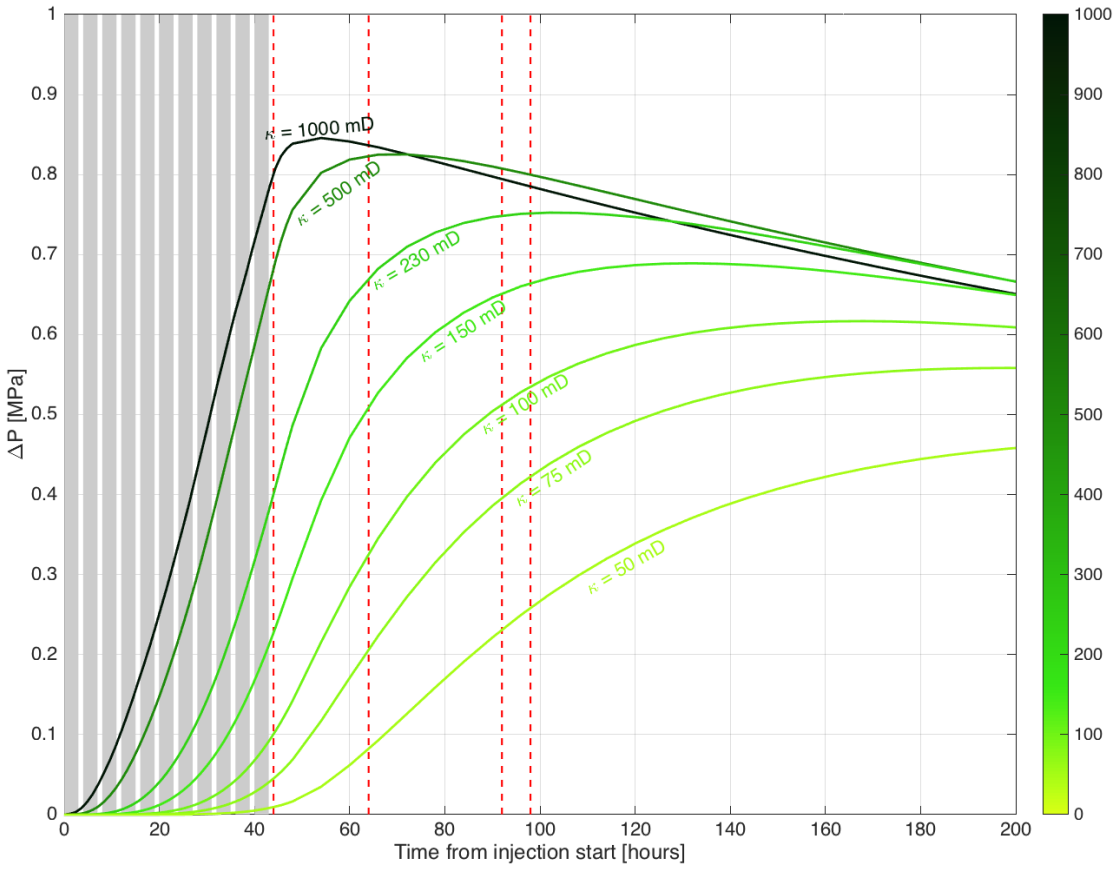

Figure 7: Modelled pore pressure increases at the distal end of the fracture corridor as a function of time, for a suite of fracture corridor permeabilities from 50 – 1,000 mD. The 11 injection stages are marked by the grey shading, while the observed reactivation times of the NS1 fault from the onset of activity on each SW fracture corridor are marked by the red dashed lines.

This range of pressure increases is much larger than that modelled by Keranen et al. (2014) for the Jones, Oklahoma earthquake swarm, but is similar to that calculated by Schoenball et al. (2018) for the Guthrie-Langston, Oklahoma, earthquakes. It is also significantly larger than static stress transfer magnitudes that have been invoked as causes for fault activation elsewhere (e.g., Pennington and Chen, 2017; Kettlety et al., 2019). Evidently, the range of pore pressure increases produced by our model, regardless of κ_{FC}, are within or above the range typically deemed sufficient to cause fault reactivation.

The time delay between the start of injection and the maximum pressure increase at the distal end of the fracture, T_{PMAX}, is smaller for higher permeabilities, with the smallest delay time of T_{PMAX} = 52 hours for κ_{FC} = 1,000 mD, and the largest delay time of T_{PMAX} = 250 hours occurring for κ_{FC} = 50 mD. Once ΔP_{MAX} has been reached, pressures gradually decrease as fluids diffuse into the non-fractured shale rock mass.

In Figure 7 the pressure increases with time are compared with the observed time delays between the onset of activity in each SW cluster and activity in the corresponding portion of the NS1 fault (Table 2). For the lower permeability cases (κ_{FC} = 50 mD and κ_{FC} = 75 mD), the changes in pore pressure after 40 hours (the shortest observed reactivation delay time) are negligible. This would appear to rule out these lower κ_{FC} models, since elevated pressures are not able to reach the fault by the time that it is observed to reactivate.

For the κ_{FC} = 1,000 mD case, pressures at the distal end of the fracture corridor increase rapidly, and have reached almost their maximum value by the shortest observed reactivation delay time (40 hours). However, the modelled pressures are decreasing by c. 90 hours, corresponding to the largest observed reactivation delay time, which would appear to rule out these models since we would expect reactivation to occur while pressures are increasing. However, the higher permeability models cannot be ruled out entirely, as delays between the reactivation trigger and the resulting seismicity have been observed (e.g., van der Elst et al., 2013), implying that the time delay between the modelled increase in pressures along the fracture zone and the observed seismicity on the fault is caused by the gradual nucleation of rupture on the fault before observed seismicity takes place.

However, the mid-range permeability models (κ_{FC} = 150 – 230 mD) show the best match to the observed reactivation delay times. The pressure has increased by a substantial amount (> 0.2 MPa) by 44 hours (the shortest observed reactivation delay period) and is continuing to increase, reaching near to the maximum by 90 – 100 hours (the longest observed reactivation delay periods). Although these permeabilities are several orders of magnitude larger than the

matrix permeability, laboratory tests of the permeability of unpropped fractures in the Montney formation of Alberta, Canada, yield even larger fracture permabilities on the order of 1-3 Darcies (Ghanizadeh et al., 2015b).

In summary, both the analytical and numerical modelling demonstrates that the observed delay times are consistent with pore pressure transfer along a fracture corridor, assuming permeability values that are consistent with observations of seismic hydraulic diffusivity made in a range of geological settings (Talwani and Acree, 1985). Numerical modelling indicates that pore pressure increases of 0.5 MPa might reasonably be expected at the fault assuming such a mechanism.

4.2. Stress transfer

Deformation and slip around Well C produced by hydraulic fracturing will affect the stress field in the surrounding rocks. If this produces Coulomb Failure Stress (CFS) increases on the NS1 fault, then this stress transfer represents a viable alternative causative mechanism for the induced seismicity. There are two potential sources for stress transfer onto the NE1 fault. The first is the tensile opening of the hydraulic fractures themselves, and the second is the seismicity occurring in each of the SW clusters.

4.2.1. Stress Transfer caused by tensile hydraulic fracture opening

The opening of the hydraulic fractures is more challenging to model, since this process is mostly aseismic (e.g., Maxwell et al., 2008), and so we do not have any observations that directly constrain either the orientations or the lengths of the hydraulic fractures, nor the amount of opening that has occurred. Instead, we appeal to an observational argument to assess whether stress transfer from hydraulic fracture opening could be causing reactivation of the NS1 fault.

Hydraulic fracturing takes place along the length of Well C from toe to heel, using a very similar injection design for each stage. We can surmise that any zones of increased CFS associated with tensile opening would also move consistently southwards as Well C is stimulated. If stress transfer from tensile hydraulic fracture opening was the cause of seismicity on the NS1 fault, then we would expect the fault to reactivate along its entirety, with the loci of seismicity moving consistently southwards along the fault. Instead, as documented in Section 3, seismicity occurs at specific points along the fault that are aligned with the SW clusters.

The behaviour of the NS1 fault during stimulation of Well C can be contrasted with the behaviour during stimulation of Well D, which is within 200 – 300 m of the fault. During

441 stimulation of Well D, the NS1 fault reactivates along its entire length, with the loci of
442 seismicity moving consistently southwards as the hydraulic stimulation moves southwards
443 along Well D, as might be expected if there is direct interaction between the hydraulic fractures
444 and the fault.

445 We also note that Westwood et al. (2017) simulated stress transfer from a suite of generic
446 hydraulic fracturing models, including tensile opening, finding that changes in the CFS at
447 distances larger than 500 m were less than 0.001 MPa, significantly less than the pore pressure
448 changes modelled in Section 4.1.

449 **4.2.2. Stress Transfer caused events in the SW clusters**

450 The alternative possibility is that slip associated with the events in the SW clusters could have
451 promoted slip on the NS1 fault. Modelling of stress transfer caused by earthquake slip is well
452 established, having its origins in understanding aftershock distribution after large tectonic
453 earthquakes (e.g. Stein et al., 1992). Here we use the PSCMP code (Wang et al., 2006) to model
454 the changes in CFS caused by the events in each of the SW clusters.

455 This modelling requires us to know the rupture dimensions for each event, and the orientation
456 of the rupture. However, such parameters can only be directly constrained for a small fraction
457 of the events with the highest signal to noise ratios (e.g., Zhang et al., 2019). Instead, we
458 approach the problem from a stochastic perspective (e.g., Verdon et al., 2015). We know the
459 position of each event, and the event magnitudes. We assign source mechanism parameters to
460 each observed event in each cluster randomly from appropriate statistical distributions. We
461 perform 1,000 model instantiations for each of the SW clusters, taking as our result the median
462 stress changes from the overall model population.

463 Zhang et al. (2019) show that all the events within the SW clusters have right-lateral strike-slip
464 mechanisms, with vertical nodal planes striking at 30^{o} (parallel to the overall cluster
465 orientations). We therefore assign nodal planes strikes with a normal distribution with a mean
466 of 30^{o} and a standard deviation of 5^{o}, dips with a normal distribution with a mean of 90^{o} and a
467 standard deviation of 5^{o}, and rakes with a normal distribution with a mean of 180^{o} and a
468 standard deviation of 5^{o}. Stress drops are assigned with a uniform distribution ranging from 0.1
469 $< \Delta\sigma <$ 10 MPa, from which the rupture dimensions and displacement are computed using the
470 event magnitude. We assume a Young's moduli of 50 GPa and a Poisson's ratio of 0.25, based
471 on values for the Duvernay observed by Soltanzadeh et al. (2015) and Weir et al. (2017).

To determine the impact on the NS1 fault, we resolve the modelled stress changes into shear and normal stresses acting on a vertical, right-lateral strike-slip fault with a strike of 5°. The results of our stress modelling – the changes in the Mohr-Coulomb criteria (Equation 2) – are plotted in Figure 8. We observe that the modelled stress changes are small, less than 0.01 MPa at the point where the first events on the NS1 fault are observed. Moreover, the events on NS1 lie within a lobe of negative CFS change, indicating that the stress changes move the NS1 feature away from, rather than towards, failure.

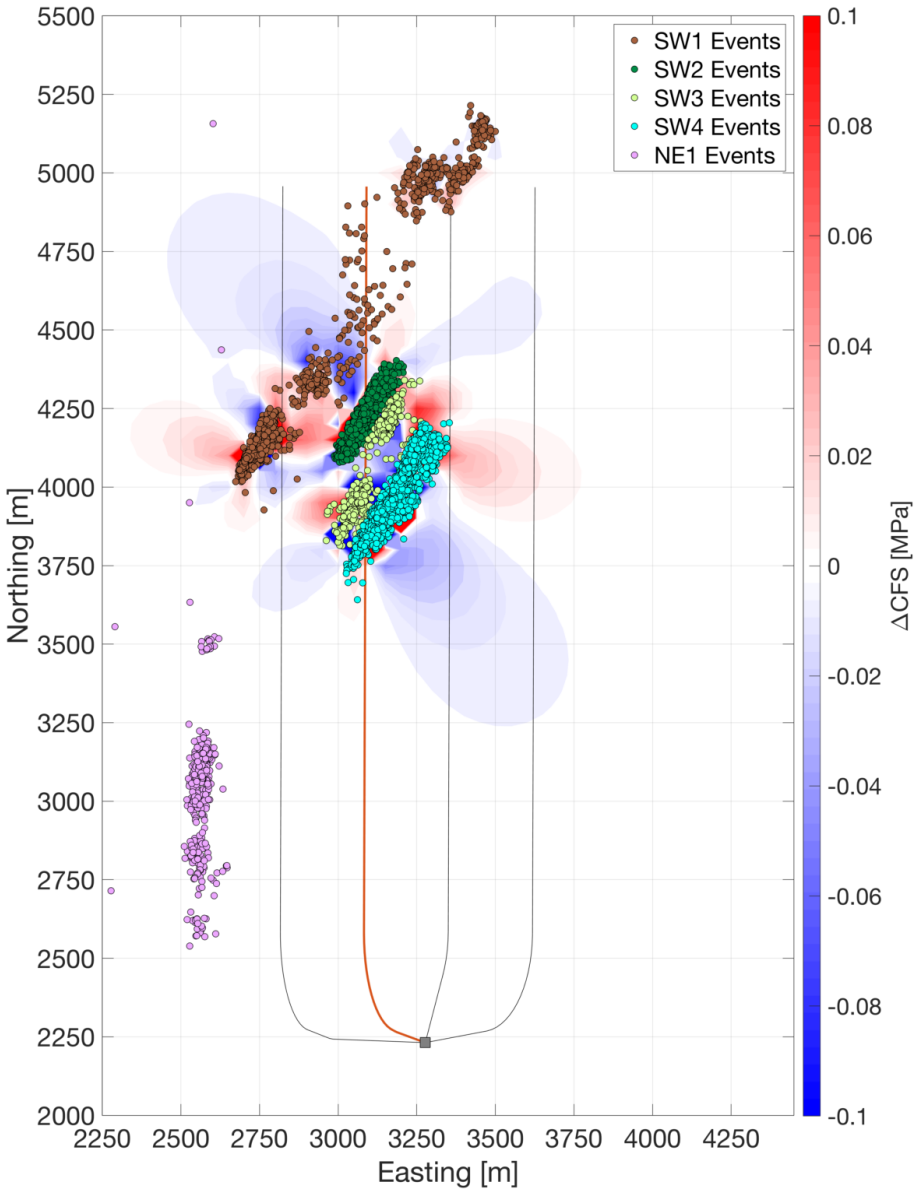

Figure 8: Changes in Mohr-Coulomb failure criteria (ΔCFS) produced by the slip of the events in the SW clusters, resolved onto the NS1 fault orientation. Here we show the cumulative change produced by all of the clusters. The impacts on the NS1 fault events (pink) are small, and actually lie within a lobe of negative ΔCFS.

The comparison between the modelled pore fluid pressure changes and the modelled stress transfer produces a clear conclusion. Our fluid flow models suggest an increase in pore pressure of approximately 0.5 MPa at the fault, which would decrease the effective normal stress acting on the fault, pushing it towards failure. In contrast, the stress transfer modelling produces a negative CFS change of less than 0.01 MPa. Therefore, it is clear the observed seismicity on the NS1 fault is driven by pore pressure transfer via a hydraulic connection, rather than by stress transfer through the rock frame.

5. Discussion and Conclusions

This dataset demonstrates the importance of local geological factors on fault reactivation during hydraulic fracturing. Reactivation of the large fault adjacent to the wells was caused by transfer of fluid pressure along pre-existing fracture networks. These fractures allowed the pressure pulse to propagate much further from the well that would be expected if the low-permeability shale rock were otherwise intact. Previous studies have suggested that events occurring larger distances from hydraulic fracturing wells must have been triggered by stress transfer. However, we show here that this may not be the case, unless the presence of pre-existing permeable pathways can be ruled out.

Eaton et al. (2018) examined the 3D/3C reflection seismic data at this site. They were able to identify faults, but found that there was little evidence for spatial correlation between faults imaged by the reflection seismic and faults reactivated by the seismicity. For example, the NS1 fault on which the largest events occurred was not expressed in the reflection seismic data, whereas large faults near to the wells imaged by the reflection seismic (e.g., F2 and F6 of Eaton et al., 2018) showed no signs of reactivation. This implies that we cannot rely on pre-drill site selection using fault "respect distances" (e.g., Westwood et al., 2017) to mitigate induced seismicity, because faults that are imaged may not reactivate, while seismic events may occur on faults that were not imaged.

If we cannot directly image faults in the subsurface then we must assume that critically-stressed faults may be distributed within a given volume of rock. If this is the case, then the probability that a given industrial activity triggers seismicity will depend on the size of the rock volume that it perturbs. In low permeability, intact shale rocks, the volume of rock affected by hydraulic fracturing will be relatively small, and therefore the probability of intersecting a critically-stressed fault would be low. However, in this study we show that the presence of pre-existing permeable fracture networks may significantly increase the volume of rock that is affected by the hydraulic fracturing, and therefore will increase the probability of causing induced seismicity. A similar case has been observed in the Cardium Formation in Alberta, Canada,

where Galloway et al. (2018) suggest that karst collapse along near-vertical faults served as a conduit for vertical stress transfer.

Various methods can be used to image subsurface fracture networks. For example, aligned fractures will create seismic anisotropy that can be imaged by seismic reflection surveys (e.g., Hall and Kendall, 2003). Once wells have been drilled, fracture networks may be imaged by borehole imaging logs. Geomechanical reconstructions can also be used to simulate the expected fracture networks (e.g., Bond et al., 2013). However, as mentioned above we cannot be sure that such methods will positively identify faults and fracture networks that may be of concern.

Therefore, our study suggests that a proactive approach to mitigating seismicity is required, where high-quality real-time microseismic monitoring is used to identify and map subsurface structures that are being perturbed by the stimulation. If an operator is able to image and understand the geomechanical impacts of their activities on adjacent faults and fracture networks, then it is possible to re-design hydraulic fracturing programs such that the likelihood of causing large events is reduced (e.g., Clarke et al., 2019). This can be done, for example, by skipping stages within wells, by adjusting pumping parameters, or by changing the properties of the injected fluids. As more detailed studies of fault activation due to hydraulic fracturing are carried out, improved methods for assessing, mitigating, and responding to induced seismicity will be developed, and the importance of a pre-existing fracture network should not be overlooked.

Acknowledgements

The ToC2ME program was enabled by generous support from two companies. Continuous raw data (geophone and broadband recordings, network code TC2ME) are available through the IRIS Data Center following a holdback period that expires on July 1, 2020. The seismicity catalog used to prepare the figures in this manuscript is provided as a Supplementary data table. Financial support was provided by Chevron and the Natural Sciences and Engineering Research Council of Canada (NSERC) through the NSERC-Chevron Industrial Research Chair in Microseismic System Dynamics. Continuous geophone data were recorded under license from Microseismic Inc. for use of the BuriedArray method. TGS is sincerely thanked for providing the 3D multicomponent seismic data used in this analysis. CGG and Seisware are thanked for providing GeoSoftware used to display and interpret the seismic data. All sponsors of the Microseismic Industry Consortium are also sincerely thanked for their ongoing support. Nadine Igonin was supported through the NSERC PGS-D, the SEG Reba C. Griffin Memorial Scholarship, and this collaboration was funded through the NSERC MSFSS. We thank

Emerson Automation Solutions for the use of their Tempest reservoir modelling tools, and specifically Paul Childs for his helpful discussions as to the application of this software. James Verdon was funded by NERC Grant NE/R018162/1. Michael Kendall was funded by NERC Grant NE/R018006/1.

References

Atkinson, G.M., D.W. Eaton, H. Ghofrani, D. Walker, B. Cheadle, R. Schultz, R. Shcherbakov, K. Tiampo, J. Gu, R.M. Harrington, Y. Liu, M. van der Baan, H. Kao, 2016. Hydraulic fracturing and seismicity in the Western Canada Sedimentary Basin: Seismological Research Letters 87, 631-647.

Bao X. and D.W. Eaton, 2016. Fault activation by hydraulic fracturing in Western Canada: Science 354, 1406-1409.

Batzle M. and Z. Wang, 1992. Seismic properties of pore fluids: Geophysics 57, 1396-1408.

Bond C.E., R. Wightman, P.S. Ringrose, 2013. The influence of fracture anisotropy on CO_2 flow: Geophysical Research Letters 40, 1284-1289.

Brace W.F., 1980. Permeability of crystalline and argillaceous rocks: International Journal of Rock Mechanics, Mining Science and Geomechanics 17, 241-251.

Caffagni E., D.W. Eaton, J.P. Jones, M. Van der Baan, 2016. Detection and analysis of microseismic events using a Matched Filtering Algorithm (MFA): Geophysical Journal International 206, 644-658.

Clarke H., L. Eisner, P. Styles, P. Turner, 2014. Felt seismicity associated with shale gas hydraulic fracturing: The first documented example in Europe: Geophysical Research Letters 41, 8308-8314.

Clarke H., E. Vaughan, M. Hampson, J.P. Verdon, T. Kettlety, A. Baird, 2019. Management of induced seismicity during hydraulic fracturing in real time: 81st EAGE Annual Conference, London, Expanded Abstracts.

Darold A., A.A. Holland, C. Chen, A. Youngblood, 2014. Preliminary analysis of seismicity near Eagleton 1-29, Carter County, July 2014: Oklahoma Geological Survey Open-File Report OF2-2014.

Deng K., Y. Liu, R.M. Harrington, 2016. Poroelastic stress triggering of the December 2013 Crooked Lake, Alberta, induced seismicity sequence: Geophysical Research Letters 43, 8482-8491.

Dunn L., G. Schmidt, K. Hammermaster, M. Brown, R. Bernard, E. Wen, R. Befus, S. Gardiner, 2012. The Duvernay Formation (Devonian): Sedimentology and reservoir characterization of a shale gas/liquids play in Alberta, Canada: GeoConvention, Calgary, Article 90174.

Eaton, D.W., 2018. Passive seismic monitoring of induced seismicity: fundamental principles and application to energy technologies. Cambridge University Press.

Eaton D.W., N. Igonin, A. Poulin, R. Weir, H. Zhang, S. Pellegrino, G. Rodriguez, 2018. Induced seismicity characterisation during hydraulic fracture monitoring with a shallow-wellbore geophone array and broadband sensors: Seismological Research Letters 89, 1641-1651.

Ekpo E., D. Eaton, R. Weir, 2017. Basement Tectonics and Fault Reactivation in Alberta Based on Seismic and Potential Field Data. In Okiweli A. (ed.), Geophysics. Intechopen, London.

Ellsworth, W. L., 2013. Injection-induced earthquakes: Science 341, 1225942-1:7.

595 Emerson 2014. Tempest Reservoir Engineering: accessed at:
596 http://www.emerson.com/documents/automation/tempest-more-data-sheet-2014-en-
597 82050.pdf on 03.08.2018.

598 Friberg P.A., G.M. Besana-Ostman, I. Dricker, 2014. Characterisation of an earthquake
599 sequence triggered by hydraulic fracturing in Harrison County, Ohio: Seismological
600 Research Letters 85, 1295-1307.

601 Galloway, E., Hauck, T., Corlett, H., Pană, D. and Schultz, R., 2018. Faults and associated karst
602 collapse suggest conduits for fluid flow that influence hydraulic fracturing-induced
603 seismicity. Proceedings of the National Academy of Sciences, 115(43), pp.E10003-E10012.

604 Ghanizadeh A., Bhowmik S., Haeri-Ardakani O., Sanei H., and Clarkson C., 2015a. A
605 comparison of shale permeability coefficients derived using multiple non-steady-state
606 measurement techniques: Examples from the Duvernay Formation, Alberta (Canada): Fuel,
607 140, 371-387.

608 Ghanizadeh A., Clarkson C., Aquino S., Ardakani O.H., and Sanei H., 2015b. Petrophysical
609 and geomechanical characteristics of Canadian tight oil and liquid-rich gas reservoirs: I.
610 Pore network and permeability characterization: Fuel, 153, 664-681.

611 Green C.A., P. Styles, B.J. Baptie, 2012. Preese Hall shale gas fracturing review and
612 recommendations for induced seismic mitigation. Department of Energy and Climate
613 Change, London.

614 Goebel, T.H.W., Weingarten, M., Chen, X., Haffener, J. and Brodsky, E.E., 2017. The 2016
615 Mw5. 1 Fairview, Oklahoma earthquakes: Evidence for long-range poroelastic triggering at
616 > 40 km from fluid disposal wells. Earth and Planetary Science Letters, 472, pp.50-61.

617 Gutenberg B., and C.F. Richter, 1944. Frequency of earthquakes in California: Bulletin of the
618 Seismological Society of America 34, 185-188.

619 Hall S.A. and J-M. Kendall, 2003. Fracture characterization at Valhall: Application of P-wave
620 amplitude variation with offset and azimuth (AVOA) analysis to a 3D ocean-bottom data
621 set: Geophysics 68, 1150-1160.

622 Heidbach, O., M. Rajabi, K. Reiter, M. Ziegler and WSM Team, 2016. World stress map
623 database release 2016, GFZ Data Services.

624 Holland A.A., 2013. Earthquakes triggered by hydraulic fracturing in south-central Oklahoma:
625 Bulletin of the Seismological Society of America 103, 1784-1792.

626 Igonin N., M. Zecevic, D.W. Eaton, 2018. Bilinear magnitude-frequency distributions and
627 characteristic earthquakes during hydraulic fracturing: Geophysical Research Letters 45,
628 12866-12874.

629 Kao H., R. Visser, B. Smith, S. Venables, 2018. Performance assessment of the induced
630 seismicity traffic light protocol for northeastern British Columbia and western Alberta: The
631 Leading Edge 37, 117-126.

632 Keranen K.M., M. Weingarten, G.A. Abers, B.A. Bekins, S. Ge, 2014. Sharp increase in central
633 Oklahoma seismicity since 2008 induced by massive wastewater injection: Science 345,
634 448-451.

635 Kettlety T., J.P. Verdon, M.J. Werner, J-M. Kendall, J. Budge, 2019. Investigating the role of
636 elastostatic stress transfer during hydraulic fracturing-induced fault reactivation:
637 Geophysical Journal International 217, 1200-1216.

638 Kozłowska, M., Brudzinski, M.R., Friberg, P., Skoumal, R.J., Baxter, N.D. and Currie, B.S.,
639 2018. Maturity of nearby faults influences seismic hazard from hydraulic fracturing.
640 Proceedings of the National Academy of Sciences, 115(8), pp.E1720-E1729.

641 Lyster S., H.J. Corlett, H. Berhane, 2017. Hydrocarbon resource potential of the Duverney
642 Formation in Alberta – Update: Alberta Energy Regulator/Alberta Geological Survey Open
643 File Report 2017-02.

644 Maxwell S.C., J. Shemeta, E. Campbell, D. Quirk, 2008. Microseismic deformation rate
645 monitoring: SPE Annual Technical Conference, Denver, SPE116596.

646 Michael A.J., 1984. Determination of stress from slip data: faults and folds: Journal of
647 Geophysical Research 89, 11517-11526.

648 Pennington C. and X. Chen, 2017. Coulomb stress interactions during the M_W 5.8 Pawnee
649 sequence: Seismological Research Letters 88, 1024-1031.

650 Schoenball M., F. R. Walsh, M. Weingarten, W.L. Ellsworth, 2018. How faults wake up: the
651 Guthrie-Langston, Oklahoma earthquakes: The Leading Edge 37, 100-106.

652 Schultz R., V. Stern, M. Novakovic, G. Atkinson, Y.J. Gu, 2015a. Hydraulic fracturing and the
653 Crooked Lake sequences: Insights gleaned from regional seismic networks: Geophysical
654 Research Letters 42, 2750-2758.

655 Schultz R., S. Mei, D. Pana, V. Stern, Y. J. Gu, A. Kim, D. Eaton, 2015b. The Cardston
656 earthquake swarm and hydraulic fracturing of the Exshaw Formation (Alberta Bakken play):
657 Bulletin of the Seismological Society of America 105, 2871-2884.

658 Schultz R., R. Wang, Y.J. Gu, K. Haug, G. Atkinson, 2017. A seismological overview of the
659 induced earthquakes in the Duvernay play near Fox Creek, Alberta: Journal of Geophysical
660 Research 112, 492-505.

661 Segall, P. and Lu, S., 2015. Injection-induced seismicity: Poroelastic and earthquake nucleation
662 effects. Journal of Geophysical Research: Solid Earth, 120(7), pp.5082-5103.

663 Shapiro S., and Dinske C., 2009. Fluid-injection seismicity: pressure diffusion and hydraulic
664 fracturing: Geophysical Prospecting, 57(2), 301-310.

665 Shipman, T., MacDonald, R. and Byrnes, T., 2018. Experiences and learnings from induced
666 seismicity regulation in Alberta. Interpretation, 6(2), pp.SE15-SE21.

667 Skoumal R.J., M.R. Brudzinski, B.S. Currie, 2015. Induced earth-quakes during hydraulic
668 fracturing in Poland Township, Ohio: Bulletin of the Seismological Society of America 105,
669 189-197.

670 Soltanzadeh M., Davies G., Fox A., Hume D., and Rahim N., 2015. Application of mechanical
671 and mineralogical rock properties to identify fracture fabrics in the Devonian Duvernay
672 formation in Alberta: Unconventional Resources Technology Conference, URTeC
673 2178289.

674 Stein R.S., G.C.P. King, J. Lin, 1992. Change in failure stress on the southern San Andreas
675 fault system caused by the 1992 magnitude = 7.4 Landers earthquake: Science 258, 1328-
676 1332.

677 Talwani P. and S. Acree, 1984. Pore pressure diffusion and the mechanism of reservoir-induced
678 seismicity: Pure and Applied Geophysics 122, 947-965.

679 Teanby N.A., J-M. Kendall, M. van der Baan, 2004. Automation of shear-wave splitting
680 measurements using cluster analysis: Bulletin of the Seismological Society of America 94,
681 453-463.

682 van der Elst N.J., H.M. Savage, K.M. Keranen, G.A. Abers, 2013. Enhanced remote earthquake
683 triggering at fluid-injection sites in the midwestern United States: Science 341, 164-167.

684 Verdon J.P., A. Wuestefeld, J.T. Rutledge, I.G. Main, J-M. Kendall, 2013. Correlation between
685 spatial and magnitude distributions of microearthquakes during hydraulic fracture
686 stimulation: 75th EAGE Conference, London, Expanded Abstracts Th-01-12.

687 Verdon J.P., A.L. Stork, R.C. Bissell, C.E. Bond, M.J. Werner, 2015. Simulation of seismic
688 events induced by CO_2 injection at In Salah, Algeria: Earth and Planetary Science Letters
689 426, 118-129.

690 Verdon J.P., J-M. Kendall, S.P. Hicks, P. Hill, 2017. Using beamforming to maximise the
691 detection capability of small, sparse seismometer arrays deployed to monitor oil field
692 activities: Geophysical Prospecting 65, 1582-1596.

693 Viegas G., T. Urbancic, and H. Chittenden, 2018. Influence of geological setting on stress
694 released by hydraulic fracture-induced earthquakes: First Break 36, 77-81.

695 Wang, R., Lorenzo Martín, F., Roth, F., 2006: PSGRN/PSCMP - a new code for calculating
696 co- and post-seismic deformation, geoid and gravity changes based on the viscoelastic-
697 gravitational dislocation theory, Computers and Geosciences, 32, 4, 527-541.

698 Wang R., Y.J. Gu, R. Schultz, A. Kim, G. Atkinson, 2016. Source analysis of a potential
699 hydraulic-fracturing-induced earthquake near Fox Creek, Alberta: Geophysical Research
700 Letters 43, 564-573.

701 Weir R., Eaton D., Lines L., Lawton D., and Ekpo E., 2017. Inversion and interpretation of
702 seismic-derived rock properties in the Duvernay play: Interpretation, 6(2), SE1-SE14.

703 Westaway R., 2017. Integrating induced seismicity with rock mechanics: a conceptual model
704 for the 2011 Preese Hall fracture development and induced seismicity: In E.H. Rutter, J.
705 Mecklenburgh, K.G. Taylor (eds) *Properties of Mudrocks*, Geological Society of London
706 Special Publications 454, 327-359.

707 Westwood R.F., Toon S.M., Styles P., Cassidy N.J., 2017. Horizontal respect distance for
708 hydraulic fracturing in the vicinity of existing faults in deep geological reservoirs: a review
709 and modelling study: Geomechanics and Geophysics for Geo-Energy and Geo-Resources
710 3, 379-391.

711 Wilson M.P., Worrall F., Davies R.J., Almond S., 2018. Fracking: How far from faults?:
712 Geomechanics, Geophysics and Geophysics for Geo-Energy and Geo-Resources 4, 193-
713 199.

714 Zhang H., D.W. Eaton, G. Rodriguez, S.Q. Jia, 2019. Source-mechanism analysis and stress
715 inversion for hydraulic-fracturing-induced event sequences near Fox Creek, Alberta:
716 Bulletin of the Seismological Society of America, 109(2), 636-651.